Cancer-associated fibroblast-derived extracellular vesicles promote pancreatic cancer progression via the RAP1B/ANLN axis

DAIGO YOSHIMORI[1,2], MITSUHIRO KUDO[1], KOUSUKE ISHINO[1], JUNJI UEDA[2], YUKAKO SHINTANI-DOMOTO[1], AKIRA MATSUSHITA[2], YOUICHI KAWANO[2], TAKASHI ONO[2], TAKAHIRO HARUNA[3], KAZUHIKO ENDO[1,2], AKIRA HAMAGUCHI[2], TAKENORI FUJII[1], YOKO KAWAMOTO[1], KIYOSHI TEDUKA[1], TAEKO KITAMURA[1], ATSUSHI MASAMUNE[4], AKIHISA MATSUDA[2], HIROSHI YOSHIDA[2] and RYUJI OHASHI[1]

[1]Department of Integrated Diagnostic Pathology, Graduate School of Medicine, Nippon Medical School, Tokyo 113-8603, Japan; [2]Department of Gastroenterological Surgery, Nippon Medical School Hospital, Tokyo 113-8603, Japan; [3]Department of Gastrointestinal Surgery, Nippon Medical School Tama Nagayama Hospital, Tokyo 206-8512, Japan; [4]Division of Gastroenterology, Tohoku University Graduate School of Medicine, Sendai 980-8575, Japan

Received March 27, 2026; Accepted July 27, 2026

DOI: 10.3892/or.2026.9182

Abstract. Pancreatic ductal adenocarcinoma (PDAC) is one of the most lethal malignancies worldwide, characterized by late diagnosis, rapid progression and resistance to conventional therapies. Cancer-associated fibroblast (CAF)-derived extracellular vesicles (EVs) contribute to PDAC progression, but their downstream molecular effectors remain unclear. In the present study, it was demonstrated that CAF-derived EVs enhanced the proliferative, migratory and invasive capacity of PDAC cells across two independent cell lines, as assessed by Cell Counting Kit-8 assays and Transwell migration and Matrigel invasion assays. RAP1B was identified as a prominently upregulated protein by label-free proteomic profiling following EV exposure. High RAP1B expression, evaluated by immunohistochemistry, in a cohort of 77 resected PDAC specimens tended to be more frequent with advancing pathological stage and was associated with poorer overall survival. RAP1B knockdown using small interfering RNA suppressed proliferation and motility in PDAC cells and induced cytokinesis failure characterized by multinucleation and cytoskeletal abnormalities, as demonstrated by time-lapse imaging and immunofluorescence staining. Proteomic profiling of RAP1B-knockdown cells identified anillin (ANLN) as a downstream mediator; ANLN knockdown recapitulated these cytokinetic defects, whereas ANLN knockdown did not reciprocally affect RAP1B levels, establishing a unidirectional RAP1B/ANLN axis. Furthermore, RAP1B depletion sensitized PDAC cells to gemcitabine, showing additive growth inhibition. In conclusion, CAF-derived EVs mediate PDAC progression via the RAP1B/ANLN axis, representing a novel and promising therapeutic target in PDAC.

Correspondence to: Mr. Daigo Yoshimori, Department of Gastroenterological Surgery, Nippon Medical School Hospital, 1-5-1 Sendagi, Bunkyo-ku, Tokyo 113-8603, Japan
E-mail: daigo-yoshimori@nms.ac.jp

Abbreviations: CAF, cancer-associated fibroblast; EV, extracellular vesicle; PDAC, pancreatic ductal adenocarcinoma; TME, tumor microenvironment; ECM, extracellular matrix; OS, overall survival; NTA, nanoparticle tracking analysis; TEM, transmission electron microscopy; siRNA, small interfering RNA; NC, negative control; CCK-8, Cell Counting Kit-8; IHC, immunohistochemistry; ANLN, anillin; MAPK, mitogen-activated protein kinase; ERK, extracellular signal-regulated kinase

Key words: PDAC, CAFs, EVs, RAP1B, anillin, cytokinesis, proteomics

Introduction

Pancreatic ductal adenocarcinoma (PDAC) is considered a globally lethal malignancy with a persistently poor prognosis. Owing to the clinically silent nature of early disease and non-specific symptoms, most patients present with advanced stages at diagnosis, and only a limited fraction (~15-20%) are considered candidates for upfront resection (1-3). In unresectable diseases, the outcomes remain dismal despite contemporary systemic therapy and radiation. Population-based estimates indicate an overall 5-year relative survival of ~12-13 and ~3% for distant diseases (4). Emerging studies have sought to identify novel prognostic biomarkers and therapeutic targets to improve patient stratification and treatment outcomes (5,6). To overcome these clinical limitations, the establishment of more effective and targeted therapeutic approaches is imperative.

In recent years, the reciprocal interactions between pancreatic cancer (PC) cells and the tumor microenvironment (TME) have been increasingly investigated. The TME comprises a

dense extracellular matrix (ECM) and diverse stromal and immune cell populations, including cancer-associated fibroblasts (CAFs), tumor-associated macrophages, and endothelial and stromal progenitor cells, that collectively regulate tumor growth, invasion, metastasis and therapeutic response (7,8). In particular, CAFs are central components of the TME, shaping a fibrotic ECM and modulating proliferative/invasive signaling and immune regulation, which influences tumor progression and therapeutic response (9,10). CAF-derived extracellular vesicles (EVs) play a key role in the intercellular communication between CAFs and PDAC cells. CAF-derived EVs can be internalized by PC cells to promote proliferation, migration/invasion, and treatment resistance (11-13). Consistent with the importance of invasion-promoting mechanisms in PDAC, a recent study identified novel molecular drivers of epithelial-to-mesenchymal transition (EMT) and cytoskeletal remodeling as key contributors to PDAC aggressiveness (14). These functional findings notwithstanding, research on the global, downstream proteomic changes induced in PC cells upon the uptake of CAF-derived EVs has been limited.

Rap1 is a Ras-related small GTPase that integrates extracellular cues to regulate integrin-dependent adhesion, cell polarity and cytoskeletal remodeling, which are processes fundamental to cancer cell motility and proliferation (15,16). Mechanistically, Rap1 activity couples to adhesion signaling and focal adhesion dynamics, influencing migration and invasion across tumor types (16,17). Previous evidence has emphasized Rap1 as a context-dependent oncogenic mediator in multiple malignancies. RAP1B, Ras-related small GTP-binding protein Rap-1b, is an isoform of human Rap1. In renal cell carcinoma (RCC), RAP1B overexpression tends to promote cell proliferation and migration by modulating MAPK/ERK signaling, while RAP1B silencing suppresses tumor growth and induces apoptosis (18). Similar pro-tumorigenic functions have also been reported in colorectal and gastric cancers (19,20). However, the precise mechanism by which RAP1B drives proliferative control in PC remains elusive, particularly in the context of the TME.

In the present study, focus was addressed on RAP1B, which was significantly upregulated and promoted proliferation in SUIT-2 cells following exposure to CAF-derived EVs. To clarify how RAP1B dictates these oncogenic behaviors, a proteomics-based approach was employed. Furthermore, the therapeutic potential of targeting RAP1B was evaluated, both as a monotherapy and in combination with standard treatments.

Materials and methods

Patients and cancer tissues. A total of 77 patients with PDAC who underwent surgical resection between May 2016 and November 2020 were identified from the archival records of Nippon Medical School Hospital (Tokyo, Japan). The present study was conducted in accordance with the 2013 Declaration of Helsinki and the Japanese Society of Pathology Ethics Committee. The present study was approved by the Nippon Medical School Hospital Institutional Review Board (approval no. M-2023-142), and the requirement for written informed consent was waived owing to the retrospective nature of the study; instead, patients were provided with the opportunity to opt out of the study. The clinicopathological stage was determined according to the TNM classification system of the American Joint Committee on Cancer. The overall survival (OS) was defined as the interval between the date of a definite diagnosis and the date of death or the last follow-up.

Cell lines and cell culture. The human PC cell lines, PANC-1 and SUIT-2, were obtained from the Japanese Collection of Research Bioresources and were cultured in RPMI-1640 (Gibco; Thermo Fisher Scientific, Inc.) supplemented with 10% fetal bovine serum (FBS; Nichirei Biosciences Inc.) at a temperature of 37˚C in a humidified 5% CO_2 atmosphere. The human pancreatic stellate cell line hPSC-5 (RCB3588) was obtained from the RIKEN Bio Resource Research Center. The cells were cultured in Dulbecco's modified Eagle's medium/Nutrient Mixture F-12 (Ham's F-12) (1:1; Gibco; Thermo Fisher Scientific, Inc.) supplemented with 10% FBS at a temperature of 37˚C in a humidified atmosphere containing 5% CO_2. hPSC-5 cells between passages 3 and 8 were used in the present study to maintain phenotypic stability.

EV isolation and experiments. The hPSC-5-derived EVs were isolated using the MagCapture™ Exosome Isolation Kit PS Ver. 2 (FUJIFILM Wako Pure Chemical Corporation; cat. no. 290-84103) in accordance with the manufacturer's instructions. For functional assays, the EVs were added to the PANC-1 and SUIT-2 cells at a final concentration of 5 μg/ml based on the protein content in the serum-free medium. The control cells received the same volume of Exosome Elution Buffer. Moreover, the cells were cultured for 48 h before performing proliferation, migration and invasion assays and for 72 h before protein extraction. Furthermore, the cells were collected by trypsinization and subsequently subjected to the experiments as described below.

Isolation of EVs from hPSC-5 cells. EVs derived from hPSC-5 cells were isolated as follows. hPSC-5 cells were seeded in 6-well plates and cultured in Dulbecco's modified Eagle's medium/Ham's F-12 (DMEM/Ham's F-12; 1:1) supplemented with 10% FBS. When the cells reached ~70-80% confluence, the culture medium was removed, and the cells were washed three times with phosphate-buffered saline (PBS) to eliminate residual serum-derived vesicles. The cells were then incubated in serum-free DMEM/Ham's F-12 (1:1) for an additional 48 h. The conditioned medium was collected and centrifuged at 1,500 x g for 10 min at 4˚C to remove cells and cellular debris, followed by centrifugation at 10,000 x g for 30 min at 4˚C to remove larger vesicles and apoptotic bodies. The resulting supernatant was concentrated using centrifugal filter units with a 100 kDa molecular weight cutoff (Amicon® Ultra Centrifugal Filter, Merck KGaA) according to the manufacturer's instructions. EVs were subsequently isolated from the concentrated supernatant using the MagCapture™ Exosome Isolation Kit PS Ver. 2 (FUJIFILM Wako Pure Chemical Corporation; cat. no. 290-84103) in accordance with the manufacturer's protocol. The isolated EVs were collected and used for downstream experiments.

Nanoparticle tracking analysis (NTA). The size distribution and particle concentration of the isolated EVs were analyzed using a NanoSight NS300 instrument (Malvern Panalytical)

equipped with a 488-nm laser and an sCMOS camera. The samples were diluted in sterile PBS (pH 7.4) to obtain a particle concentration within the recommended range (~$1x10^8$ to $1x10^9$ particles/ml). Each sample was injected into the sample chamber using a syringe pump at a constant flow rate. For each sample, three 60-sec videos were recorded under controlled temperatures. Moreover, the videos were analyzed using NTA software (version 3.4; Malvern Panalytical) with the detection threshold set to the default value as per the manufacturer's instructions. Furthermore, the resulting data provided the mean particle size and concentration of EVs.

Transmission electron microscopy (TEM). The EV samples were diluted at a ratio of 1:10 in 0.22-μm-filtered PBS, and 4 μl of the diluted suspension was placed onto carbon-coated 200-mesh copper grids (Nisshin EM Co., Ltd.; EM grid, cat. no. 645) and allowed to adsorb for 10 min at room temperature. The grids were subsequently floated on a drop of 2% uranyl acetate solution for 1 min, followed by two washes on drops of 0.22-μm-filtered PBS. The excess stain was removed using a filter paper, and the grids were air-dried at room temperature. The grids were stored at room temperature in the dark until observation. TEM was performed using a JEM-1400Plus transmission electron microscope (JEOL, Ltd.) at magnifications ranging from x50,000 to x150,000.

Fluorescent labeling of hPSC-5-derived EVs and uptake in SUIT-2. The EVs derived from the hPSC-5 cells were fluorescently labeled using the ExoSparkler Exosome Membrane Labeling Kit-Green (EX01; Dojindo Laboratories, Inc.) in accordance with the manufacturer's instructions. Purified EVs were incubated with the dye solution for 30 min at 37˚C in the dark, and the excess dye was removed using the provided filtration tube. The SUIT-2 cells were seeded at $2.5x10^4$ cells per well in an 8-well chamber slide (Nunc Lab-Tek Chamber Slide System; cat. no. 177402PK; Thermo Fisher Scientific, Inc.) and incubated for 24 h to allow cell attachment. Subsequently, the culture medium was replaced with serum-free medium, while the cells were washed twice with PBS before adding the labeled EVs. A total of 4 h after adding the EVs, the cells were washed twice with PBS, fixed, counterstained with DAPI (10 μg/ml), and mounted for imaging. The fluorescence images were acquired using an all-in-one fluorescence microscope (BZ-X810; Keyence Corporation). The EV dye fluorescence was captured using a GFP filter set (Ex 470/40 nm; DM 495 nm; Em 525/50 nm). The DAPI fluorescence was captured using a DAPI filter set (Ex 405 nm; Em 420-480 nm). As a control, PBS underwent the same labeling and purification procedure and was added to the SUIT-2 cells instead of the EVs.

Transfection of small interfering RNA (siRNA). siRNA-mediated knockdown of RAP1B and ANLN was performed in PANC-1 and SUIT-2 cells using Silencer™ Select Validated siRNAs (Thermo Fisher Scientific, Inc.) and Lipofectamine® RNAiMAX reagent according to the manufacturer's instructions. Cells were transfected with 5 nM siRNA and incubated for 48 or 72 h before downstream analyses. Detailed information on siRNAs is provided in Table SI.

RNA extraction and reverse transcription-quantitative PCR (RT-qPCR). The total RNA was extracted using the NucleoSpin® RNA Plus (Takara Bio, Inc.), and 1 μg of RNA was reverse-transcribed using the SuperScript VILO cDNA Synthesis Kit (Thermo Fisher Scientific, Inc.) in accordance with the manufacturer's instructions. RT-qPCR analysis was performed on a Step One Plus Real-Time PCR System (Thermo Fisher Scientific, Inc.) using TaqMan Gene Expression Assays for 18S (Hs03928990_g1), RAP1B (Hs04275955_g1), and ANLN (Hs01122612_m1) with the TaqMan Fast Universal PCR Master Mix (Thermo Fisher Scientific, Inc.). Moreover, the thermal cycling conditions were 20 sec at 95˚C, followed by 40 cycles of 1 sec at 95˚C and 20 sec at 60˚C. Relative mRNA expression was measured using the $2^{-\Delta\Delta Cq}$ method (21), with 18S rRNA as an internal control. All experiments were performed in triplicate.

Protein extraction and western blotting. The total protein was extracted using urea/thiourea buffer containing 7 M urea (Wako Pure Chemical Industries, Ltd.), 2 M thiourea (Nacalai Tesque, Inc.), 3% 3-(3-[cholamidopropyl]-dimethylammonio)-1-propanesulfonate (Dojindo Molecular Technologies, Inc.), and 1% Triton X-100 (Sigma-Aldrich; Merck KGaA) from the cells. The protein concentration was measured using the Pierce® 660-nm Protein Assay Reagent (Thermo Fisher Scientific, Inc.). Western blotting was performed as previously described (22). For the sample preparation, 10 μg of protein from each cell lysate and EV samples corresponding to 1 μg of protein from hPSC-5-derived EVs were separated by electrophoresis on 5-20% SDS-polyacrylamide gradient gels (e-PAGEL®, ATTO Corporation). The antibodies used for western blotting are listed in Table SII.

Label-free proteomic analysis. Label-free proteomics was performed as previously described (23), with some modifications. A total of 4.1 mM dithiothreitol (DTT) and 54.2 mM iodoacetamide (IAM) were added to the samples, including 10 μg proteins, and a trypsin enzyme (Promega Corporation) was added to enzymatically hydrolyze for 16 h at 37˚C. The resulting peptides were treated with a GL-Tip SDB (7820-11200, GL Sciences) and subsequently dissolved in 50 μl loading buffer (0.1% formic acid and 5% acetonitrile). The eluent was evaporated in a vacuum concentrator centrifuge (Spin Dryer Lite, VC-36R, TAITEC; GCD-051X, ULVAC Kiko Inc.; VA-250F; TAITEC Corporation), and the residue was resuspended in 0.1% formic acid/5% acetonitrile. Moreover, the sample was filtered using an Ultrafree-MC membrane centrifuge filtration unit (hydrophilic PTFE; 0.2-μm pore size; cat. no. UFC30LG00; MilliporeSigma). The flow-through fraction was used in the following proteomic analysis.

In the proteomic analyses, two different nanoLC-MS/MS platforms were used due to an equipment upgrade during the study period. The peptide samples from the EV-treated cells were analyzed using the TripleTOF 5600+ system, whereas those from the siRap1B-treated cells were analyzed using the ZenoTOF 7600 system. For the analysis of the peptide samples from the EV-treated cells, a nanoLC-MS/MS system was composed of an Eksigent nanoLC Ekspert 415 (SCIEX) coupled to a TripleTOF 5600+ mass spectrometer (SCIEX).

Aliquots of the samples (equivalent to 1 μg of protein) were injected via an injector valve into a nanoLC Trap ChromXP C18 column (cat. no. 5016752; 350 μm ID x0.5 mm; 3 μm; 120 Å; SCIEX) for the desalting and concentrating peptides. After washing the trapping column, the peptides were loaded into a nano ESI spray column (NTCC-360/75-3-105; 75 nmID x100 mm; 3 μm; Nikkyo Technos). The mobile phase comprised solution A (0.1% formic acid in water) and solvent B (0.1% formic acid in acetonitrile). Subsequently, the samples were loaded with solution A at a flow rate of 2 μl/min for 10 min and eluted from the analytical column with a concentration gradient of acetonitrile from 2%B to 32%B over 120 min at a flow rate of 300 nl/min. The source conditions were optimized for the microflow rates as follows: Ion spray voltage floating of 2,300 V, nebulizing gas (GS1) of 20 psi, heating gas (GS2) of 0 psi, curtain gas (CUR) of 20 psi, interface heater temperature (TEM) of 150˚C, declustering potential (DP) of 80 V, and collision energy (CE) of 10 eV. A TOF survey scan experiment (250 msec) was conducted, acquiring from m/z 400-1,250. Information-dependent acquisition (IDA) was used for MS/MS analysis with the top 10 candidate ions collected per cycle. The MS/MS spectra were acquired from m/z 100-1,600 at an accumulation time of 100 msec with a CE of 35 eV, collision energy spread of 15 eV, ion release delay of 30, and ion release width of 15. The gradient-eluted peptides were acquired in a data-dependent manner.

For the analysis of the peptide samples from siRap1B-treated cells, a nanoLC-MS/MS system was composed of an ACQUITY UPLC M-Class System (Waters Corporation) coupled to a ZenoTOF 7600 mass spectrometer (SCIEX). Aliquots of the samples (equivalent to 200 ng of protein) were injected via an injector valve into a nanoEase M/Z Symmetry C18 trap column (180 μm x20 mm; 5 μm; 100 Å; cat. no. 186008821; Waters Corporation) for the desalting and concentrating peptides. After washing the trap column, the peptides were loaded onto a nanoEase M/Z HSS C18 T3 analytical column (75 μm x100 mm; 1.8 μm; 100 Å; cat. no. 186008815; Waters Corporation) by valve switching. The column oven temperature was set to 35˚C. The mobile phase comprised solvent A (0.1% formic acid in water) and solvent B (0.1% formic acid in acetonitrile). The samples were loaded with 1% solvent B at a flow rate of 5 μl/min for 6 min and eluted using a linear gradient from 2 to 30% solvent B over 90 min at a flow rate of 300 nl/min. The source conditions were optimized for microflow rates as follows: CUR, 25 psi; CAD gas, 7 psi; nano, 1, 10 psi; nano cell temperature, 200˚C; spray voltage, 3,000 V; DP, 80 V; and CE, 10 V. The gradient-eluted peptides were analyzed using Zeno IDA, generally referred to as data-dependent acquisition. The TOF MS survey scans were acquired over an m/z range of 400-1,250 with an accumulation time of 250 msec. Subsequently, up to 40 precursor ions with charge states of 2-5 and intensities greater than 100 counts were selected for CID fragmentation. The MS/MS spectra were acquired over an m/z range of 100-1,500 with an accumulation time of 50 msec using rolling CE. The Zeno trap was activated with a threshold of 100,000 cps, while the time-bins-to-sum was set to 8 with all the channels enabled. Database searches were performed against the SwissProt Homo sapiens database (2023_02) using Mascot v2.8.2, with trypsin specified as the digestion enzyme and a maximum of two missed cleavages permitted. Carbamido-methylation of cysteine was set as a fixed modification, and oxidation of methionine was set as a variable modification. The peptide mass tolerance was set to ±50 ppm and the MS/MS fragment ion tolerance to ±0.05 Da. Proteins identified by a minimum of two unique peptides were retained for quantification.

Each sample was assessed in triplicate. All MS/MS spectra data were searched against the SwissProt Homo sapiens database (https://www.uniprot.org/) (2023_02) using Mascot v2.8.2 (Matrix Science). The relative spectral count (Rsc) values were computed as log2-based normalized spectral-count ratios with a correction factor (f=1.25), as previously described (24). Proteins with |Rsc|≥1 (corresponding to a ≥2-fold increase or ≤0.5-fold decrease) were considered differentially abundant (25). A Kyoto Encyclopedia of Genes and Genomes (KEGG) pathway enrichment analysis was performed using the DAVID Bioinformatics Resources (version 6.8; https://david.ncifcrf.gov), with the KEGG pathway knowledgebase as background (26). Differentially expressed proteins (fold-change ≥2.0 or ≤0.5) were subjected to functional enrichment and pathway analyses using MetaboAnalyst version 6.0 (www.metaboanalyst.ca) and ShinyGO version 0.85 (http://bioinformatics.sdstate.edu/go/).

Cell proliferation assay. Cell proliferation was assessed using the Cell Counting Kit-8 (CCK-8; Dojindo Laboratories, Inc.) in accordance with the manufacturer's instructions. Cells were seeded in 96-well plates at a density of $5x10^3$ cells per well and incubated under standard conditions. CCK-8 solution (10 μl to each well containing 100 μl of culture medium) was added at the indicated time points (24, 48, 72 and 96 h), and absorbance at 450 nm was measured using a microplate reader (Infinite® F50; Tecan Group, Ltd.) after 2 h of incubation at 37˚C.

Transwell migration and invasion assay. Cell migration was assessed using 8-μm pore Transwell inserts (Corning, Inc.). Cell invasion was assessed using Transwell inserts coated with Matrigel (BD Biosciences) at 37˚C for 2 h. For migration assays, $1x10^5$ cells were seeded in the upper chamber in serum-free medium, whereas for invasion assays, $2x10^5$ cells were seeded on Matrigel-coated inserts. The lower chamber was filled with RPMI-1640 containing 10% FBS as a chemoattractant. After 24 h (migration) or 48 h (invasion) of incubation, the non-migratory cells were removed by cotton swab, and the cells on the lower surface of the membrane were fixed with methanol, stained with crystal violet (FUJIFILM Wako Pure Chemical Corporation), and counted in five random fields per insert using a BZ-X810 microscope (Keyence Corporation) at x200 magnification.

Time-lapse imaging. For time-lapse imaging, cells were seeded in 24-well plates and allowed to adhere for 24 h. Phase-contrast images were acquired every 30 min for 72 h using a BZ-X810 all-in-one fluorescence microscope (Keyence Corporation) with a built-in incubation chamber maintained at 37˚C and 5% CO_2. Cell numbers and cell area were determined by automated image analysis using Cellpose (27) and analyzed using custom scripts. A total of 5 fields per condition were analyzed.

Immunofluorescence staining. Cells were seeded on glass coverslips, transfected with siRNA for 72 h, fixed with 4% paraformaldehyde for 15 min, permeabilized with 0.1% Triton X-100 for 5 min, and blocked with 1% bovine serum albumin (BSA) for 30 min. F-actin was stained with Alexa Fluor 594-conjugated phalloidin (1:1,000; cat. no. A12381; Thermo Fisher Scientific, Inc.) for 30 min at room temperature. Nuclei were counterstained with DAPI (10 μg/ml). Fluorescence images were acquired using the BZ-X810 microscope (Keyence Corporation) at x300 magnification.

Immunohistochemistry (IHC). IHC staining was performed on 4-μm formalin-fixed, paraffin-embedded tissue sections using an anti-RAP1B antibody. Formalin-fixed, paraffin-embedded tissue sections (4-μm thick) were used for IHC staining of RAP1B. After deparaffinization, antigen retrieval was performed by autoclaving the sections at 121˚C for 5 min in 10 mM sodium citrate buffer (pH 6.0). Endogenous peroxidase activity was blocked by incubation in 0.3% hydrogen peroxide in methanol for 30 min at room temperature. The sections were then incubated overnight at 4˚C with a primary antibody against RAP1B (mouse polyclonal antibody; 1:200 dilution; cat. no. 10840-1-AP; Proteintech Group, Inc.) diluted in phosphate-buffered saline containing 1% BSA. After washing, the sections were incubated with Simple Stain MAX-PO (R) (Nichirei Biosciences, Inc.) for 40 min at room temperature. Immunoreactivity was visualized using 0.02% diaminobenzidine containing 0.003% hydrogen peroxide for 2 min. The sections were counterstained with Mayer's hematoxylin, dehydrated, and mounted for microscopic evaluation.

The degree of immunostaining was measured by multiplying the proportion score by the intensity score. The proportion score was defined as follows: 0, no positive immunoreactive cells; 1, ≤30% positive immunoreactive cells; 2, 31-60% positive immunoreactive cells; or 3, >60% positive immunoreactive cells. The intensity score was defined as follows: 0, no immunoreactivity; 1, weak immunoreactivity; 2, intermediate immunoreactivity; or 3, strong immunoreactivity. The immunostaining score could take one of seven discrete values (0, 1, 2, 3, 4, 6, or 9). For the subsequent analyses, cases with a score of ≤3 (at or below the midpoint) were classified as the low-expression group, whereas those with a score of ≥4 were classified as the high-expression group. To analyze associations between expression levels and clinicopathological features, tumor tissues from 77 patients were assessed. Two pathologists independently assessed all scores.

Combined treatment of gemcitabine and RAP1B knockdown. Gemcitabine was dissolved in DMSO and diluted with serum-free medium to the indicated concentrations, with the final DMSO concentration adjusted to 0.1% (v/v) in all treatment conditions. For the 0 nM control, an equivalent volume of DMSO was added. PANC-1 and SUIT-2 cells were seeded at $5x10^3$ cells per well in 96-well plates and allowed to adhere for 24 h, after which the medium was replaced with gemcitabine-containing medium. Cell viability was assessed at the indicated time points using the CCK-8 (Dojindo Laboratories, Inc.). For combination experiments, cells were suspended in medium containing 5 nM siRAP1B and seeded at $5x10^3$ cells per well. After 24 h, the medium was replaced with gemcitabine-containing medium, and this time point was defined as 0 h. Four replicate wells were analyzed per condition.

Statistical analysis. All quantitative data are presented as the mean ± SEM. Comparisons between two groups were performed using an unpaired Student's t-test, and comparisons among multiple groups were conducted using one-way analysis of variance. Associations between RAP1B expression and clinicopathological parameters were analyzed using the chi-square test, with the chi-square test for trend applied to ordered categorical variables; for variables in which more than 20% of the cells had expected counts of less than 5, Fisher's exact test and an exact trend test (Cochran-Armitage) were used instead. Survival was analyzed using the Kaplan-Meier method, and differences between survival curves were assessed using the log-rank test. $P<0.05$ was considered to indicate a statistically significant difference. All statistical analyses were performed using GraphPad Prism version 10 (GraphPad Software, Inc.; Dotmatics) or IBM SPSS Statistics version 32.0.0 (IBM Corp.).

Results

hPSC-5-derived EVs promote proliferation, migration and invasion of PC cells. The hPSC-5 cells exhibited a spindle-shaped morphology (Fig. 1A) and expressed α-SMA, a myofibroblastic CAF marker, vimentin and fibronectin, which are characteristic markers of activated stellate cells and CAFs. The expression of Meflin, a cancer-restraining CAF marker, and IL-6, an inflammatory CAF marker, was not observed (Fig. 1B). The EVs exhibited a vesicle-like bilayer structure based on TEM images (Fig. 1C). Their size was ~50-100 nm (mean ± SD, 72.4±3.0 nm), as determined by NTA using NanoSight® (Fig. 1D). Western blotting confirmed the presence of the EV markers CD9, CD63 and CD81 (Fig. 1E). These findings confirmed the successful isolation of hPSC-5-derived EVs.

Fluorescence microscopy revealed that the labeled EVs were internalized by SUIT-2 cells (Fig. 1F). It was next investigated how the uptake of these EVs altered the biological behavior of PC cells. Proliferation assays indicated increased cell proliferation in both SUIT-2 and PANC-1 cells treated with hPSC-5-derived EVs compared with the control group (Fig. 1G and J). Invasion and migration assays revealed increased migration and invasion in SUIT-2 cells (Figs. 1H and I; S1A) and increased invasion in PANC-1 cells (Figs. 1K and L; S1B).

Proteomic identification of RAP1B as a key effector of hPSC-5-derived EVs and its functional role in PC cells. Proteomic profiling of SUIT-2 cells exposed to hPSC-5-derived EVs identified a total of 3,123 proteins, among which 188 proteins were significantly upregulated (Rsc >1), and 114 were significantly downregulated (Rsc <-1) (Table SIII). KEGG pathway analysis using the DAVID Bioinformatics Resources revealed significant enrichment of multiple cancer-related pathways, including the ErbB signaling pathway (hsa04012), RCC pathway (hsa05211) and focal adhesion pathway (hsa04510) (Fig. 2A). Among the differentially expressed

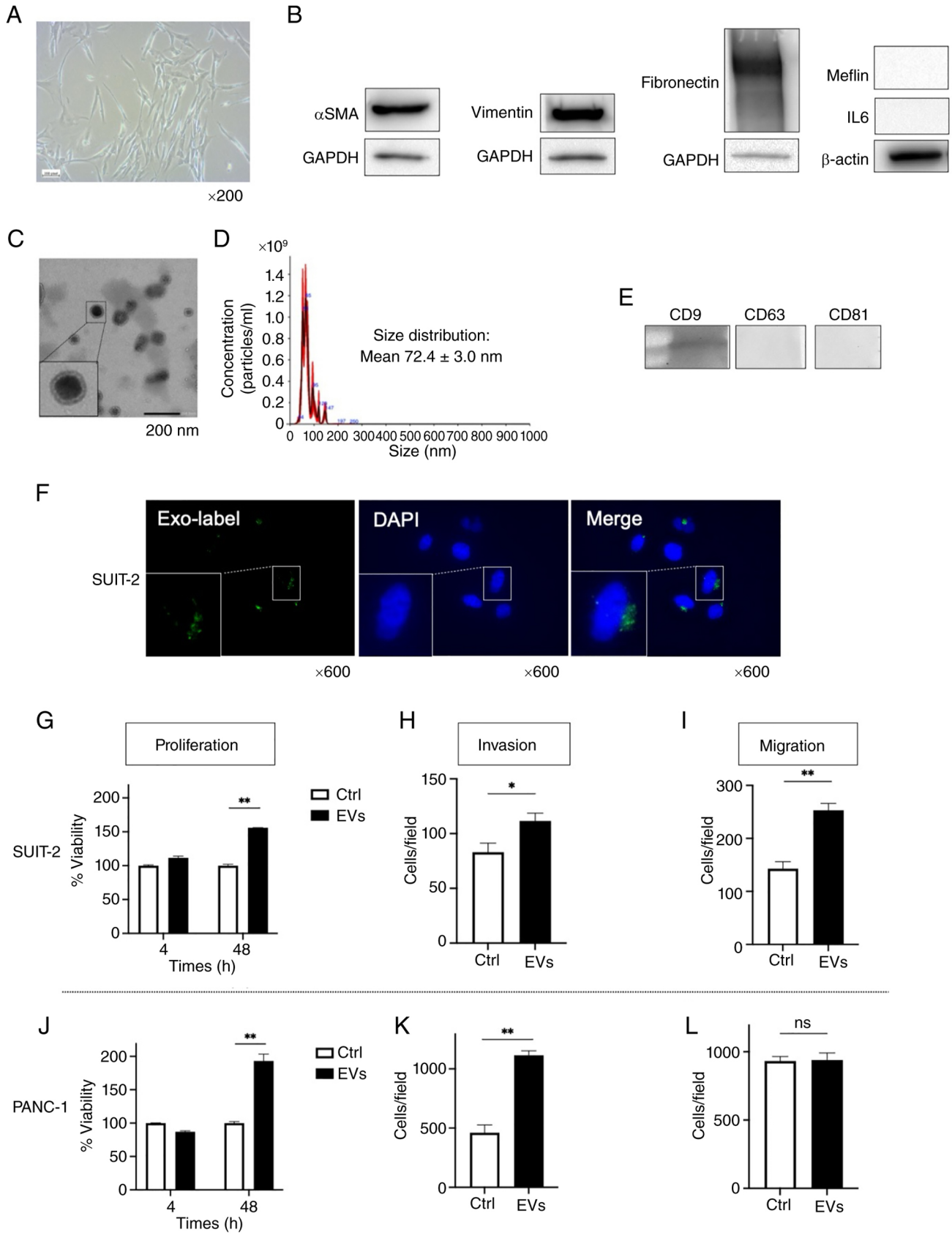

Figure 1. hPSC-5-derived EVs promote proliferation, migration and invasion of pancreatic cancer cells. (A) Phase-contrast microscopic image of hPSC-5 cells. Magnification, x200. (B) Western blot analysis of classical cancer-associated fibroblast markers in hPSC-5 cells. GAPDH was used as the loading control for α-SMA, vimentin and fibronectin, as α-SMA (~42 kDa) comigrates with β-actin (~42 kDa) on the same membrane. β-actin was used as the loading control for Meflin and IL-6, which were assessed on a separate membrane. (C) Transmission electron microscopy image of purified hPSC-5-derived EVs obtained by negative staining. (D) Size distribution of hPSC-5-derived EVs analyzed by nanoparticle tracking analysis (NanoSight®). (E) Western blot analysis confirming the presence of classical EV markers (CD9, CD63 and CD81) in hPSC-5-derived EVs. (F) Fluorescent labeling of hPSC-5-derived EVs and their uptake by SUIT-2 cells. Magnification, x600. (G-L) Effects of hPSC-5-derived EVs on (G and J) proliferation, (H and K) migration and (I and L) invasion in SUIT-2 and PANC-1 cells. Data are expressed as the mean ± SEM. *P<0.05 and **P<0.01 vs. Ctrl. EVs, extracellular vesicles; ns, not significant.

A

KEGG pathway name	$-\log_{10}(p)$	Fold enrichment
hsa03420: Nucleotide excision repair	3.65	6.39
hsa03013: Nucleocytoplasmic transport	3.57	4.66
hsa05211: Renal cell carcinoma	3.40	5.84
hsa05164: Influenza A	2.70	3.24
hsa04144: Endocytosis	2.41	2.62
hsa04371: Apelin signaling pathway	2.21	3.26
hsa05220: Chronic myeloid leukemia	1.77	3.98
hsa05170: Human immunodeficiency virus 1 infection	1.61	2.38
hsa04012: ErbB signaling pathway	1.58	3.55
hsa04935: Growth hormone synthesis, secretion and action	1.50	2.94
hsa03030: DNA replication	1.47	5.60
hsa04810: Regulation of actin cytoskeleton	1.43	2.20
hsa01100: Metabolic pathways	1.42	1.34
hsa04720: Long-term potentiation	1.37	3.76
hsa00830: Retinol metabolism	1.35	3.70
hsa04664: Fc epsilon RI signaling pathway	1.35	3.70
hsa05219: Bladder cancer	1.33	4.91
hsa04510: Focal adhesion	1.32	2.23

B

Up-regulated		Down-regulated	
Uniprot ID	Rsc	Uniprot ID	Rsc
EF1A3_HUMAN	5.20	K2C6C_HUMAN	-5.03
RAP1B_HUMAN	4.21	K2C74_HUMAN	-3.02
ST134_HUMAN	3.89	H33_HUMAN	-3.02
H14_HUMAN	2.76	ADX_HUMAN	-2.45
FRMD8_HUMAN	2.41	RS27_HUMAN	-2.45

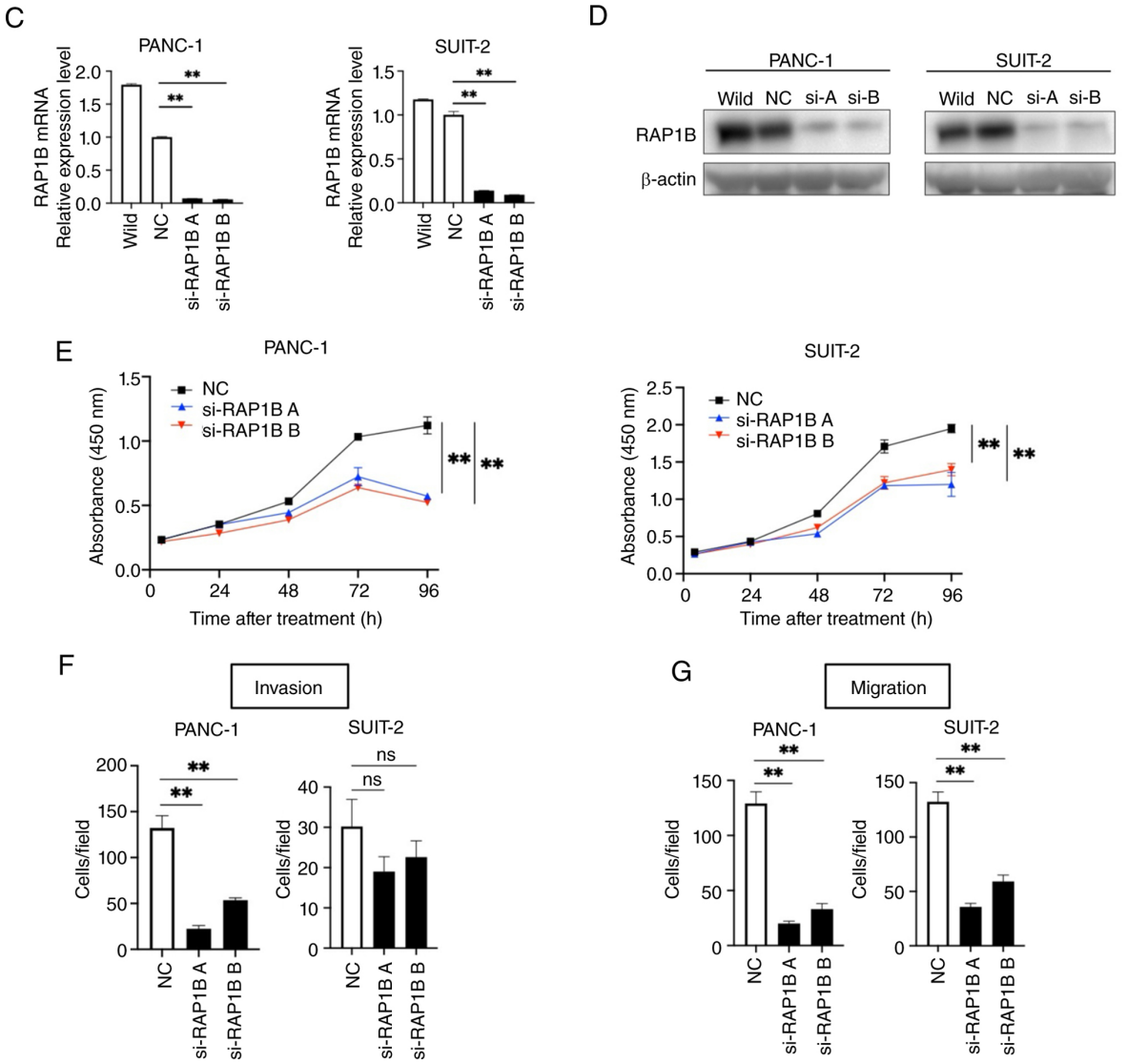

Figure 2. Proteomic identification of RAP1B as a key effector of hPSC-5-derived EVs and its functional role in pancreatic cancer cells. (A) KEGG pathway analysis of significantly altered proteins was performed using DAVID; pathways with P<0.05 are shown. (B) The top five upregulated and downregulated proteins identified in the proteomic analysis. (C and D) PANC-1 and SUIT-2 cells were transfected with RAP1B siRNAs (si-RAP1B A and si-RAP1B B; 5 nM) using Lipofectamine RNAiMAX. Knockdown efficiency was evaluated by (C) reverse transcription-quantitative PCR and (D) western blotting. (E) Cell Counting Kit-8 assays were performed to assess the proliferation of PANC-1 and SUIT-2 cells with RAP1B knockdown or negative control. (F and G) Transwell invasion and migration assays performed in PANC-1 and SUIT-2 cells after RAP1B knockdown. Data are expressed as the mean ± SEM. **P<0.01 vs. NC. KEGG, Kyoto Encyclopedia of Genes and Genomes; si-, small interfering; ns, not significant; NC, negative control.

proteins, RAP1B exhibited the second-highest absolute Rsc value, highlighting it as a prominent EV-responsive candidate (Fig. 2B). To functionally validate the role of RAP1B, siRNA-mediated RAP1B knockdown was performed using two independent siRNAs (si-RAP1B A and B). Both siRNAs efficiently suppressed RAP1B expression at the mRNA and

protein levels in SUIT-2 and PANC-1 cells compared with the negative control (Fig. 2C and D). RAP1B knockdown significantly inhibited cell proliferation in both cell lines, as assessed by the CCK-8 assay (Fig. 2E). In addition, RAP1B knockdown significantly reduced migration in SUIT-2 and PANC-1 cells and reduced invasion in PANC-1 cells, as demonstrated by invasion and migration assays (Figs. 2F and G; S2A and B). These results indicate that RAP1B is a key downstream effector mediating the pro-tumorigenic effects of hPSC-5-derived EVs in PC cells.

Identification of ANLN as a downstream effector of RAP1B and its functional role in PC cells. Since RAP1B has been implicated in the modulation of MAPK/ERK signaling in renal cell carcinoma (18) and in an oncogenic axis associated with EMT marker expression in PDAC (28), these pathways were first examined by western blotting following RAP1B knockdown (Fig. S3). RAP1B knockdown increased the p-ERK/ERK ratio in both PANC-1 and SUIT-2 cells and the p-p38/p38 ratio in PANC-1 cells, whereas the EMT-related markers E-cadherin, N-cadherin and vimentin showed inconsistent changes between the two cell lines. To investigate the molecular mechanisms underlying RAP1B knockdown-induced changes in biological behaviors, including proliferation, migration and invasion, a proteomic analysis was performed in PANC-1 cells. A total of 2,015 proteins were identified, among which 59 were significantly upregulated (>1.0-fold), and 142 were significantly downregulated (<-1.0-fold) following RAP1B knockdown (Table SIV). Gene Ontology (GO) enrichment analysis using proteins with significantly decreased expression revealed significant enrichment of molecular functions related to cadherin binding, cell adhesion molecule binding, structural molecule binding and cytoskeletal protein binding (Fig. 3A, Tables SV-SVII). Among the proteins contributing to these enriched GO terms, the six most significantly downregulated candidates are shown in Fig. 3B. As an additional criterion for candidate prioritization, the association between mRNA expression levels of these six proteins and OS was examined using The Cancer Genome Atlas data accessed via the OncoLnc platform (http://www.oncolnc.org/) (n=174). ANLN, CTNNA1 and CKAP5 demonstrated a significant association with OS, whereas VPS25, PDCD5 and CALM1 did not (Fig. S4). Moreover, RAP1B knockdown consistently reduced ANLN expression at both the mRNA and protein levels in PANC-1 and SUIT-2 cells (Fig. 3C and D). In addition, the proteomic dataset showed that LASP1, a reported downstream effector of ANLN (29), was also decreased following RAP1B knockdown, in parallel with the reduction in ANLN (Fig. S5). Based on these combined results, ANLN was selected for subsequent functional analyses. To verify that RAP1B acts upstream of ANLN (and not vice versa), RAP1B expression was assessed after ANLN knockdown. ANLN knockdown using two independent siRNAs (si-ANLN A and B) did not affect RAP1B mRNA levels in either PANC-1 or SUIT-2 cells (Fig. 3E), indicating that RAP1B regulates ANLN expression and that ANLN knockdown does not reciprocally affect RAP1B levels.

To assess the functional role of ANLN in PC, ANLN was knocked down using siRNA, and its effects on cell proliferation, migration and invasion were evaluated. Two independent siRNAs efficiently reduced ANLN expression at both the mRNA and protein levels compared with the negative control (Fig. 3F and G). ANLN knockdown significantly suppressed proliferation in both PANC-1 and SUIT-2 cells (Fig. 3H and I). In addition, ANLN knockdown significantly reduced migration and invasion in PANC-1 cells and reduced invasion in SUIT-2 cells (Figs. 3J and K; S6A and B).

RAP1B/ANLN axis regulates cytokinesis and cytoskeletal organization in PC cells. To clarify the cellular basis of the reduced proliferation induced by RAP1B and ANLN knockdown, cell division dynamics and morphology were analyzed using time-lapse imaging and cytoskeletal analyses. Time-lapse analysis revealed that RAP1B knockdown markedly impaired mitotic progression in both PANC-1 and SUIT-2 cells. RAP1B-knockdown cells entered mitosis but frequently failed to complete cytokinesis, resulting in prolonged mitotic duration, reduced mitotic frequency, and the accumulation of enlarged, binucleated, or multinucleated cells [Fig. 4A and B; Video S1]. These cells also exhibited reduced migratory activity and progressive cell enlargement over time. Consistent with these observations, fixed-point analyses demonstrated a significant reduction in overall cell proliferation (Fig. 4C and E), primarily due to mitotic failure and decreased division frequency, along with a significant increase in mean cell area at 72 h (Fig. 4D and F). As a consequence, RAP1B-knockdown cells remained sparse throughout the observation period, whereas control cells approached near confluence.

To determine whether ANLN knockdown recapitulates the phenotypes induced by RAP1B knockdown, time-lapse imaging was similarly performed following ANLN knockdown. ANLN-knockdown cells exhibited frequent cytokinesis failure in both PANC-1 and SUIT-2 cells, leading to the persistent formation of enlarged multinucleated cells [Fig. 4G and H, Video S2]. Fixed-point analyses confirmed a significant reduction in cell proliferation (Fig. 4I and K) and an increase in mean cell area (Fig. 4J and L), consistent with the phenotypes observed after RAP1B knockdown.

To further characterize the underlying cytoskeletal alterations, immunofluorescence staining for F-actin and nuclei was performed (Fig. 4M). In control cells, F-actin was evenly distributed throughout the cytoplasm, with prominent accumulation at the contractile ring during cytokinesis (arrowheads). By contrast, both RAP1B- and ANLN-knockdown cells exhibited pronounced cell enlargement and multinucleation (asterisks) accompanied by aberrant F-actin organization. Abnormal accumulation of F-actin was frequently observed around the nuclei and between nuclei in multinucleated cells (arrows), indicating defective contractile ring formation and disorganized cytoskeletal architecture. Collectively, these findings demonstrate that the RAP1B/ANLN axis plays a critical role in regulating cytokinesis and cytoskeletal organization in PC cells.

Clinicopathological features of RAP1B expression and enhanced antitumor effects of gemcitabine combined with RAP1B knockdown. RAP1B expression was evaluated by IHC in a cohort of 77 PC specimens with corresponding clinicopathological data. Kaplan-Meier survival analysis demonstrated

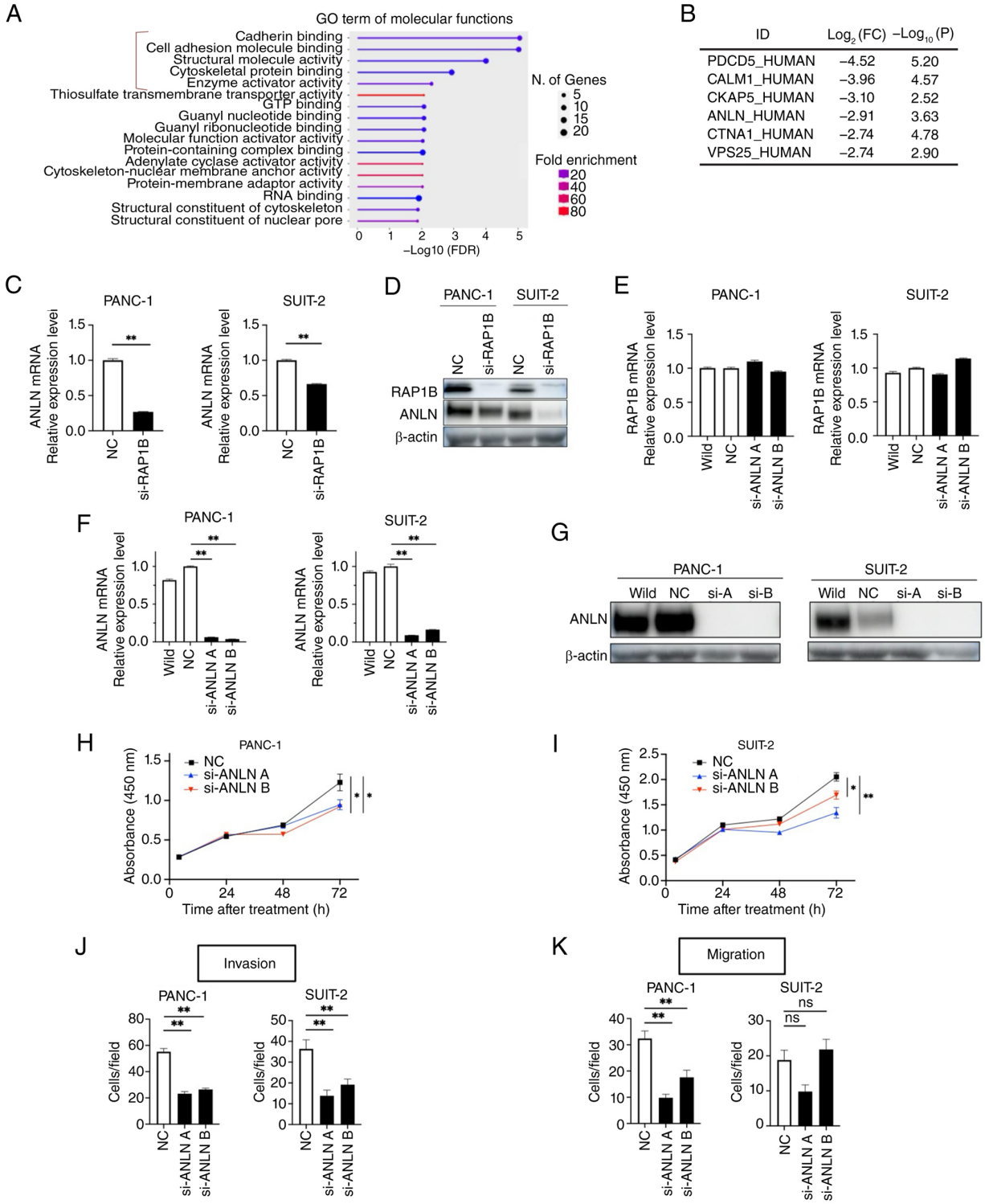

Figure 3. Identification of ANLN as a downstream effector of RAP1B and its functional role in pancreatic cancer cells. (A) GO-MF enrichment analysis of significantly downregulated proteins following RAP1B knockdown. (B) The top six significantly downregulated proteins contributing to the five most enriched GO-MF terms. (C and D) ANLN mRNA (C) and protein (D) expression levels in PANC-1 and SUIT-2 cells following RAP1B knockdown. (E) RAP1B mRNA levels following ANLN knockdown with two independent siRNAs (si-ANLN A and si-ANLN B; 5 nM) in PANC-1 and SUIT-2 cells. (F and G) PANC-1 and SUIT-2 cells were transfected with ANLN siRNAs (si-ANLN A and si-ANLN B; 5 nM) using Lipofectamine RNAiMAX. Knockdown efficiency was evaluated by (F) reverse transcription-quantitative PCR and (G) western blotting. (H and I) Cell Counting Kit-8 assays assessing proliferation in (H) PANC-1 and (I) SUIT-2 cells after ANLN knockdown. (J and K) Transwell invasion (J) and migration (K) assays performed in PANC-1 and SUIT-2 cells following ANLN knockdown. Data are expressed as the mean ± SEM. *P<0.05 and **P<0.01 vs. NC. ANLN, anillin; GO, Gene Ontology; MF, molecular function; si-, small interfering; ns, not significant; NC, negative control.

that patients with high RAP1B expression had significantly poorer OS than those with low RAP1B expression. The median OS was significantly shorter in the RAP1B-high group compared with the RAP1B-low group (32.0 vs. 86.0 months; HR=2.556, 95% CI: 1.324-4.938, P=0.0037; Fig. 5A and B). Clinicopathological correlation analysis revealed no significant

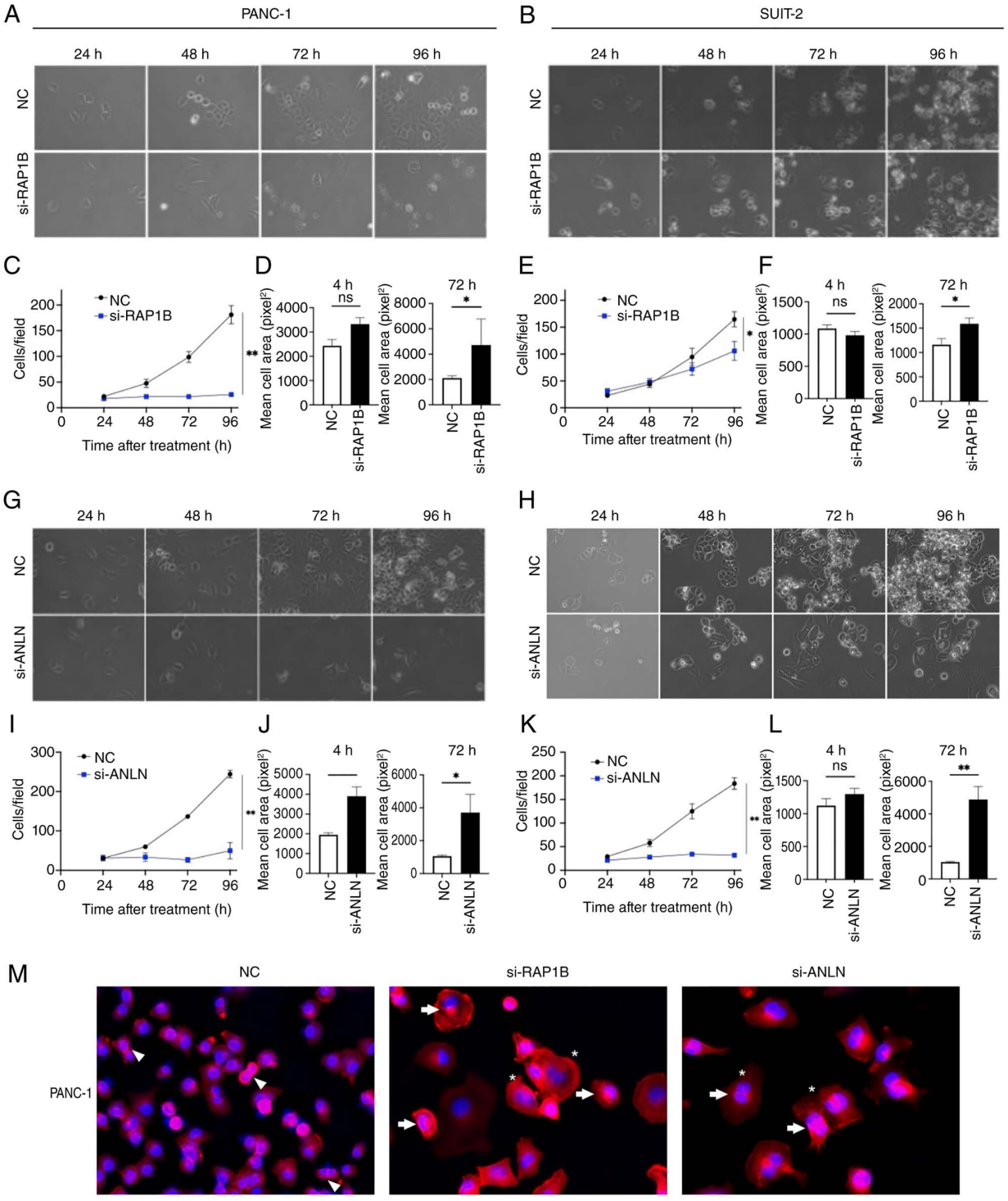

Figure 4. RAP1B/ANLN axis regulates cytokinesis and cytoskeletal organization in pancreatic cancer cells. (A and B) Time-lapse images from fixed fields of si-RAP1B and NC groups in (A) PANC-1 and (B) SUIT-2 cells: Magnification, x200. (C and E) Time course of cell numbers determined by fixed-point counts across five fields per condition. (D and F) Mean cell area determined by fixed-point counts across five fields per condition at 24 and 72 h. (G and H) Time-lapse images from fixed fields of si-ANLN and NC groups in (G) PANC-1 and (H) SUIT-2 cells: Magnification, x200. (I and K) Time course of cell numbers determined by fixed-point counts across five fields per condition. (J and L) Mean cell area determined by fixed-point counts across five fields per condition at 24 and 72 h. (M) Immunofluorescence staining of nuclei (DAPI, blue) and F-actin (red) in PANC-1 cells following RAP1B or ANLN knockdown and in NC cells: Magnification, x300. Arrowheads, arrows, and asterisks indicate representative features. Arrowheads indicate prominent F-actin accumulation consistent with the contractile ring in dividing cells. Arrows indicate aberrant F-actin accumulation around and between nuclei. Asterisks denote multinucleated or binucleated cells. Data are expressed as the mean ± SEM. *P<0.05 and **P<0.01 vs. NC. ANLN, anillin; ns, not significant; NC, negative control.

association between RAP1B expression and pathological stage by Fisher's exact test (P=0.4088; Table I); however, the exact trend test was significant (P=0.0405), suggesting that the proportion of tumors with high RAP1B expression tended to increase with advancing pathological stage. No significant associations were observed with age, sex, tumor differentiation, T or N category, lymphovascular invasion, or perineural invasion.

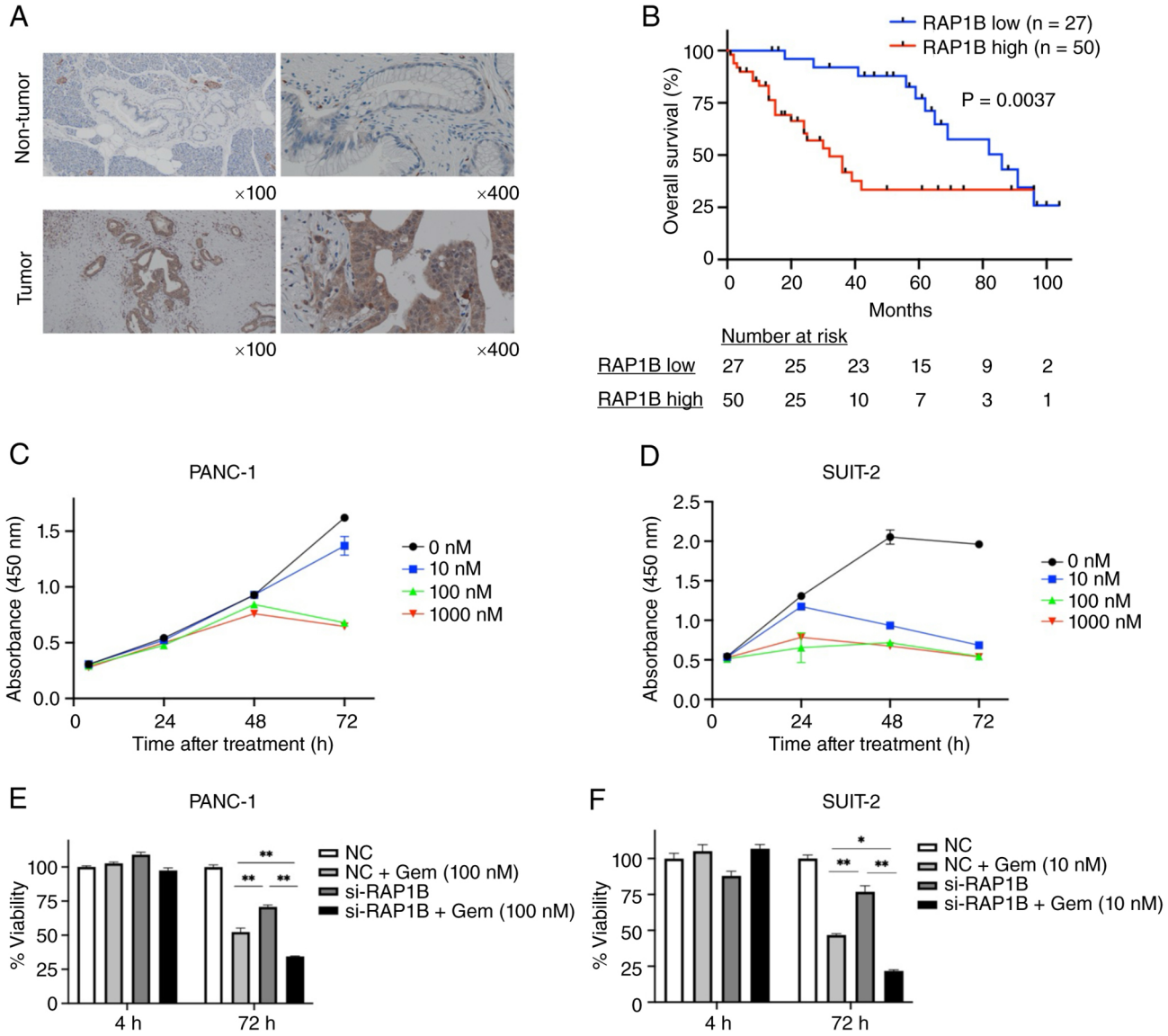

Figure 5. Clinicopathological features of RAP1B expression and enhanced antitumor effects of gemcitabine combined with RAP1B knockdown. (A) Representative immunohistochemical staining of RAP1B in pancreatic cancer tissues. (B) Kaplan-Meier curves for overall survival stratified by RAP1B expression (high vs. low). Differences between groups were assessed using the log-rank test. Tick marks indicate censored cases. The number of patients at risk is shown below the graph. (C and D) CCK-8 assay of gemcitabine response in (C) PANC-1 and (D) SUIT-2 cells. Cells were treated with 0, 10, 100, or 1, 000 nM gemcitabine; the 0 nM group received DMSO at the same final concentration as gemcitabine-treated groups. (E and F) Relative cell viability at 4 and 72 h in (E) PANC-1 and (F) SUIT-2 cells across treatment groups. The NC and si-RAP1B groups received DMSO at the same final concentration as the gemcitabine-treated groups. Cell viability was calculated as 100 x OD/OD(NC), where OD is the CCK-8 absorbance. Data are expressed as the mean ± SEM. *P<0.05 and **P<0.01. CCK-8, Cell Counting Kit-8; si-, small interfering; NC, negative control.

Given the clinical relevance of RAP1B expression, it was next evaluated whether RAP1B knockdown could enhance the antitumor efficacy of gemcitabine. At 72 h after treatment, gemcitabine alone inhibited cell proliferation in PANC-1 cells at concentrations of 100 nM or higher (Fig. 5C) and in SUIT-2 cells at concentrations of 10 nM or higher (Fig. 5D). Based on these results, 100 nM gemcitabine for PANC-1 cells and 10 nM for SUIT-2 cells were selected for subsequent experiments. As shown in Fig. 5E and F, RAP1B knockdown or gemcitabine treatment alone significantly suppressed cell proliferation compared with the negative control. Remarkably, the combination of RAP1B knockdown and gemcitabine resulted in the greatest reduction in cell proliferation in both PANC-1 and SUIT-2 cells, exceeding the effects of either treatment alone.

Discussion

In recent years, the PDAC TME has been characterized by dense desmoplasia and diverse stromal cell populations. Among these, the CAFs include functional subsets such as myofibroblastic CAFs (myCAFs) and inflammatory CAFs (iCAFs), as well as restraining CAFs (rCAFs) with tumor-suppressive properties (30-32). For example, Meflin/ISLR-positive CAFs represent a tumor-restraining subset and have been associated with improved treatment responsiveness (31,32). The characterization of hPSC-5 as a representative CAF model is an important consideration for interpreting the findings of the present study. The CAF line hPSC-5 used in the present study was originally established from PC tissue and exhibits

Table I. Associations between RAP1B expression and clinicopathological characteristics of patients with pancreatic ductal adenocarcinoma.

Variable	All cases	Expression level of RAP1B		P-value	
		Low	High	Test of association	Test for trend
Age				0.1599[a]	NA
≤70	34	9	25		
>70	43	18	25		
Sex				0.6042[a]	NA
Male	43	14	29		
Female	34	13	21		
Tumor differentiation				0.5580[b]	0.3821[d]
Well	17	8	9		
Moderate	53	17	36		
Poor	7	2	5		
T category				0.5580[b]	0.3821[d]
1	14	6	8		
2	50	17	33		
3	12	4	8		
4	1	0	1		
N category				0.2855[a]	0.13[c]
0	23	11	12		
1	28	9	19		
2	26	7	19		
Pathological stage				0.4088[b]	0.0405[d]
IA	6	4	2		
IB	13	6	7		
IIA	4	1	3		
IIB	30	10	20		
III	21	6	15		
IV	3	0	3		
Lymphovascular invasion				0.6908[b]	N/A
Negative	7	3	4		
Positive	70	24	46		
Perineural invasion				>0.999[b]	N/A
Negative	5	2	3		
Positive	72	25	47		

Statistical tests: [a]chi-square test; [b]Fisher's exact test; [c]chi-square test for trend; [d]exact trend test (Cochran-Armitage). Exact tests ([b], [d]) were used where >20% of cells had expected counts <5. Tests of association disregard category ordering, whereas tests for trend evaluate a monotonic ordered association. All tests were two-sided. N/A, not applicable.

a fibroblast-like, spindle-shaped morphology with a finite proliferative capacity. These cells have been widely used as CAFs based on their expression of classical CAF markers. In indirect co-culture systems, hPSC-5 cells have been reported to exert pro-tumorigenic effects on PC cell behavior, comparable to those of CAFs derived independently from pancreatic tumor tissues (33-35). Consistent with a myCAF phenotype, hPSC-5 cells showed no detectable expression of IL-6, an iCAF marker, or Meflin, a cancer-rCAF marker, as assessed by western blotting, but were positive for α-SMA.

CAF functions are frequently mediated by secretory signaling via EVs/exosomes. For instance, annexin A6-positive CAF-derived EVs promote PC cell migration, invasion and metastasis (36). Similarly, hypoxic PSC-derived exosomal microRNAs (miRNAs or miRs) promote proliferation and invasion through the PTEN/AKT pathway (37), whereas CAF-derived exosomal miRNA repertoires can promote gemcitabine resistance, partly by suppressing PTEN (38). In the present study, hPSC-5-derived EVs promoted proliferation, migration and invasion in both SUIT-2 and PANC-1

cells. Consistent with these phenotypic changes, KEGG pathway enrichment analysis of the proteomic data identified pathways related to cell proliferation, adhesion and migration. According to the KEGG pathway maps, Rap1 functions as an intermediate molecule in focal adhesion signaling (hsa04510) (39), where it regulates downstream JNK signaling to promote cell proliferation. In addition, within the RCC pathway (hsa05211) (40), Rap1 is implicated in regulating cell-cell junction dynamics, migration and invasion. Among the significantly upregulated proteins, RAP1B exhibited the second-highest absolute Rsc value, ranking below only EF1A3. Although EF1A3 (also known as eEF1A1) showed the highest Rsc value, it is a well-characterized translational elongation factor whose upregulation in cancer is considered a broad, non-specific response to increased translational demand rather than a cancer-specific oncogenic driver, making it a less compelling target for functional investigation. The remaining top candidates, ST134, H14 and FRMD8, are proteins whose roles in EV-mediated intercellular signaling in PDAC are not well established. By contrast, RAP1B, an isoform of Rap1, has well-documented roles in integrin inside-out signaling, focal adhesion dynamics, cell adhesion and cytoskeletal remodeling, processes directly relevant to the pro-tumorigenic phenotypes observed in the present study. Despite this prominent upregulation and biological plausibility, the role of RAP1B in PC has been only sparsely investigated, and its functional significance remains incompletely understood. Therefore, focus was addressed on RAP1B upregulation induced by hPSC-5-derived EVs in SUIT-2 cells.

RAP1B is a small GTPase that regulates integrin inside-out signaling and focal adhesion dynamics, thereby governing cell adhesion, polarity and motility (41). In PDAC, an EGFR-Src-p130CAS module promotes metastasis by activating Rap1 (42). In line with this, the long non-coding RNA LINC00514 functions as a competing endogenous RNA for miR-28-5p to upregulate RAP1B, driving PC cell proliferation, migration and invasion (28). Beyond the pancreas, RAP1B tends to promote invasive behaviors across various malignancies. For instance, in hepatocellular carcinoma, it promotes invasion and migration by upregulating TWIST1 (43). Moreover, in esophageal squamous cell carcinoma, RAP1B binds to DVL2 to activate Wnt/β-catenin signaling, thereby promoting growth, migration and metastasis (44). Collectively, these findings across multiple cancer types underscore the oncogenic potential of RAP1B. In line with this, the current data indicate that RAP1B promotes the aggressive phenotype of PC cells. Importantly, beyond its established roles in proliferation and migration, a novel role for RAP1B in cytokinesis was identified. Time-lapse and immunofluorescence analyses demonstrated that RAP1B depletion results in multinucleation, cell enlargement, and cytoskeletal disorganization. Proteomic profiling of RAP1B-knockdown cells subsequently identified ANLN as a downstream effector associated with these defects.

ANLN functions as a key coordinator of cytokinesis by recruiting division-related components, including F-actin, myosin II and septins, to the cleavage furrow, thereby acting as a central organizer of the contractile machinery, since its inhibition resulted in cytokinesis failure and cell multinucleation (45,46). High ANLN expression is associated with a poor prognosis in patients with PDAC. Its knockdown in PC cells has been shown to suppress proliferation, colony formation, migration, invasion and tumorigenicity (29,47). In the present study, it was found that ANLN expression was downregulated upon RAP1B knockdown. ANLN knockdown phenocopies the effects of RAP1B depletion, specifically, multinucleation, cell enlargement and aberrant F-actin accumulation. Furthermore, the RAP1B mRNA levels remained unaffected by ANLN knockdown, collectively supporting a unidirectional regulatory axis in which RAP1B acts upstream of ANLN. These findings support a model in which the RAP1B/ANLN axis modulates PDAC proliferation and motility by regulating cytokinesis and cytoskeletal remodeling. Notably, ANLN has also been implicated in broader oncogenic signaling pathways in PDAC. An ANLN-EZH2-miR-218-5p-LASP1 signaling axis has been reported to drive PDAC aggressiveness, whereby ANLN upregulation increases EZH2 expression, suppresses miR-218-5p, and derepresses LASP1, ultimately promoting proliferation and invasion (29). Consistent with these findings, the present proteomic analysis of RAP1B-knockdown cells revealed significant downregulation of both ANLN and LASP1 (Fig. S5), suggesting that RAP1B may function as an upstream regulator of this oncogenic axis in PDAC.

Although the present study establishes that RAP1B acts upstream of ANLN, the detailed mechanism by which RAP1B regulates ANLN expression remains largely unresolved, both in the present data and in the existing literature. To gain further insight into the signaling consequences of RAP1B depletion, several downstream pathways were examined by western blotting (Fig. S3). RAP1B knockdown increased the p-ERK/ERK ratio in both PANC-1 and SUIT-2 cells and the p-p38/p38 ratio in PANC-1 cells, indicating activation of MAPK signaling, whereas EMT markers showed inconsistent changes across cell lines. At first glance, the increase in ERK phosphorylation accompanied by reduced proliferation may appear paradoxical. However, this is consistent with the concept of ERK as a 'double-edged sword', in which excessive or sustained ERK activation can be detrimental, triggering growth arrest, senescence, or apoptosis (48). As both cell lines harbor an activating KRAS G12D mutation and already exhibit elevated baseline ERK activity, hyperactivation of this pathway has been shown to paradoxically impair proliferation in KRAS-mutant pancreatic cells (49,50). Mechanistically, Rap1 has been proposed to restrain Raf-1 activation by diluting oncogenic RAS within nanoclusters (51); loss of RAP1B may therefore push ERK activity beyond an optimal threshold into a growth-suppressive range. Notably, ANLN and MAPK signaling appear mutually associated, as ANLN silencing reduces ERK activation in other cancers (52,53), suggesting an interconnected rather than strictly linear relationship. Nevertheless, the specific transcription factors or intermediates coupling RAP1B to ANLN expression remain to be identified and represent an important direction for future research.

The potential therapeutic benefit of modulating RAP1B, both alone and in combination with conventional chemotherapy, was assessed. RAP1B knockdown alone and gemcitabine alone suppressed PC cell proliferation, whereas their combination produced the greatest growth inhibition with an additive effect. Mechanistically, gemcitabine, which

is a deoxycytidine analog, primarily targets replicating DNA and induces S-phase accumulation by inhibiting DNA synthesis and inactivating ribonucleotide reductase, which is consistent with its S-phase-specific activity (54). By contrast, RAP1B deficiency, in coordination with ANLN reduction, impairs cytokinesis and G2/M-phase progression. Moreover, these distinct inhibitory mechanisms at different cell cycle checkpoints are likely attributed to the additive growth inhibition observed with the combination treatment.

However, the present study has several limitations that need to be addressed. First, because only a single CAF line was used, it was not possible to determine whether CAF heterogeneity (for example, myCAF, iCAF and rCAF subsets) leads to distinct EV cargo profiles that differentially influence RAP1B expression in PC cells. hPSC-5 cells exhibit a myCAF-like phenotype, as evidenced by α-SMA expression and the absence of Icaf (IL-6) and rCAF (Meflin) markers, and have been widely used as a representative CAF model in previous studies of stromal-tumor interactions in PC, with pro-tumorigenic effects comparable to those reported for primary CAF isolates. Nevertheless, whether EVs derived from iCAF or rCAF subtypes similarly upregulate RAP1B or exert opposing effects remains to be investigated. Future studies incorporating primary CAF isolates or multiple CAF subtypes will be essential to address this question. Second, RAP1B activation and the precise causal mechanisms linking RAP1B and ANLN at both transcriptional and translational levels need to be assessed. Third, although KEGG pathway enrichment analysis identified multiple cancer-relevant pathways in the proteomic dataset, functional interrogation of all enriched pathways was beyond the scope of the present study. In particular, the potential contributions of pathways such as ErbB signaling (hsa04012) and nucleotide excision repair (hsa03420) to the pro-tumorigenic effects of CAF-derived EVs remain to be experimentally validated. Future studies systematically interrogating these pathways will be necessary to fully elucidate the systems-level mechanisms underlying CAF-derived EV-mediated PDAC progression. Fourth, beyond gemcitabine, the efficacy of combining RAP1B inhibition with other clinical regimens, such as FOLFIRINOX or nab-paclitaxel/gemcitabine, requires further investigation. Furthermore, the clinical analysis has inherent limitations. The cohort of 77 patients is relatively small, and multivariate Cox regression was not performed due to the limited number of events relative to potential covariates, which would risk overfitting. Accordingly, the prognostic findings should be regarded as exploratory rather than confirmatory, and validation in a larger, multicenter cohort will be necessary to establish RAP1B as an independent prognostic factor. Finally, *in vivo* validation or organoid-based experiments were not performed. Future studies employing xenograft tumor models, orthotopic implantation models, or patient-derived organoid systems will be essential to confirm the tumor-promoting role of the RAP1B/ANLN axis in a physiologically relevant context and to evaluate the therapeutic feasibility of targeting this pathway, including its combination with gemcitabine and other clinical regimens.

In conclusion, the present study provides several novel insights into the molecular mechanisms underlying CAF-mediated PDAC progression. First, it was demonstrated that CAF-derived EVs upregulate RAP1B expression in PDAC cells, thereby enhancing their proliferative, migratory, and invasive capacity. Second, through proteomic profiling, we identify a previously unrecognized RAP1B/ANLN axis that governs cytokinesis and cytoskeletal organization in PDAC cells, extending the known functions of RAP1B beyond adhesion signaling to mitotic regulation. Third, high RAP1B expression in resected PDAC specimens tended to be more frequent with advancing pathological stage and was associated with poorer overall survival, suggesting its potential utility as a prognostic biomarker, albeit in an exploratory cohort. Finally, RAP1B depletion sensitized PDAC cells to gemcitabine, producing additive growth inhibition through complementary cell cycle-targeting mechanisms. Collectively, these findings identify the RAP1B/ANLN axis as a candidate therapeutic vulnerability in PDAC. Future studies employing *in vivo* models will be essential to establish the translational feasibility of targeting this axis and to fully realize its potential as a therapeutic strategy in this disease.

Acknowledgements

Not applicable.

Funding

No funding was received.

Availability of data and materials

The data generated in the present study are included in the figures and/or tables of this article.

Authors' contributions

DY, MK and KI designed the experiments. DY, TF, YokK, KT, TK and KE performed the experiments and analyzed the data. DY, JU, AkirM, TO, TH and AH collected and analyzed the clinical samples. AtM provided the hPSC-5 cell lines. HY, RO, YSD, AtM, YouK and AkihM contributed to the conception and design of the study and to the interpretation of the data. DY, MK and KI drafted the manuscript. YouK, AkihM, HY, RO and YSD critically revised the manuscript for important intellectual content. DY and MK confirm the authenticity of all the raw data. All authors read and approved the final version of the manuscript.

Ethics approval and consent to participate

The present study was conducted according to the Declaration of Helsinki and the Japanese Society of Pathology and was approved by the Ethics Committee of Nippon Medical School Hospital (approval no. M-2023-142; Tokyo, Japan). Owing to the retrospective nature of the study, the requirement for written informed consent was waived by the Ethics Committee, and consent was obtained using an opt-out method.

Patient consent for publication

Not applicable.

Competing interests

The authors declare that they have no competing interests.

References

1. Kwaśniewska D, Fudalej M, Nurzyński P, Badowska-Kozakiewicz A, Czerw A, Cipora E, Sygit K, Bandurska E and Deptała A: How a patient with resectable or borderline resectable pancreatic cancer should be treated-a comprehensive review. Cancers (Basel) 15: 4275, 2023.
2. Farnes I, Kleive D, Verbeke CS, Aabakken L, Issa-Epe A, Småstuen MC, Labori KJ and Waage A: Resection rates and intention-to-treat outcomes in borderline and locally advanced pancreatic cancer: Real-world data from a population-based, prospective cohort study (NORPACT-2). BJS Open 7: zrad137, 2023.
3. Peshin S, Takrori E, Kodali NA, Bashir F and Singal S: Advances in the management of pancreatic cancer: current strategies and emerging therapies. Int J Mol Sci 26: 7055, 2025.
4. Siegel RL, Kratzer TB, Giaquinto AN, Sung H and Jemal A: Cancer statistics, 2025. CA Cancer J Clin 75: 10-45, 2025.
5. Lyu G and Li D: ZP3 expression in pancreatic adenocarcinoma: Its implications for the prognosis and therapy. Protein Pept Lett 32: 124-138, 2025.
6. Kaviyaprabha R, Miji TV, Sreelakshmi PS, Muthusami S, Arulselvan P and Bharathi M: Unveiling the potential role of hesperetin and emodin as a combination therapy to inhibit the pancreatic cancer progression against the C-Met gene. Protein Pept Lett 32: 280-298, 2025.
7. Hartupee C, Nagalo BM, Chabu CY, Tesfay MZ, Coleman-Barnett J, West JT and Moaven O: Pancreatic cancer tumor microenvironment is a major therapeutic barrier and target. Front Immunol 15: 1287459, 2024.
8. Ma B, Zhang DJ, Hu Y, Chen X, Gong R, Lei K, Yu Q and Ren H: HCST expression distinguishes immune-hot and immune-cold subtypes in pancreatic ductal adenocarcinoma. Curr Gene Ther 25: 62-71, 2025.
9. Wang X, Shinjyo K, Kumegawa K, Maruyama R, Mii S, Shiraki Y, Asai N, Enomoto A and Nagata H: Transgelin defines pro-tumorigenic cancer-associated fibroblasts in pancreatic cancer. Br J Cancer 134: 577-588, 2026.
10. Sahai E, Astsaturov I, Cukierman E, DeNardo DG, Egeblad M, Evans RM, Fearon D, Greten FR, Hingorani SR, Hunter T, *et al*: A framework for advancing our understanding of cancer-associated fibroblasts. Nat Rev Cancer 20: 174-186, 2020.
11. Guo Y, Li H and Sun C: Exosomal miR-125b-5p derived from cancer-associated fibroblasts promotes the growth, migration, and invasion of pancreatic cancer cells by decreasing adenomatous polyposis coli (APC) expression. J Gastrointest Oncol 14: 1064-1076, 2023.
12. Zhang P, Wang Q, Lu W, Zhang F, Wu D and Sun J: NNT-AS1 in CAFs-derived exosomes promotes progression and glucose metabolism through miR-889-3p/HIF-1α in pancreatic adenocarcinoma. Sci Rep 14: 6979, 2024.
13. Qi R, Bai Y, Li K, Liu N, Xu Y, Dal E, Wang Y, Lin R, Wang H, Liu Z, *et al*: Cancer-associated fibroblasts suppress ferroptosis and induce gemcitabine resistance in pancreatic cancer cells by secreting exosome-derived ACSL4-targeting miRNAs. Drug Resist Updat 68: 100960, 2023.
14. Luo X and Gao Z: MARVELD1 promotes the invasiveness in pancreatic adenocarcinoma through the activation of epithelial-to-mesenchymal transition. Protein Pept Lett 32: 224-233, 2025.
15. Looi CK, Hii LW, Ngai SC, Leong CO and Mai CW: The role of Ras-associated protein 1 (Rap1) in cancer: Bad actor or good player? Biomedicines 8: 334, 2020.
16. Shah S, Brock EJ, Ji K and Mattingly RR: Ras and Rap1: A tale of two GTPases. Semin Cancer Biol 54: 29-39, 2019.
17. Bos JL, de Bruyn K, Enserink J, Kuiperij B, Rangarajan S, Rehmann H, Riedl J, de Rooij J, van Mansfeld F and Zwartkruis F: The role of Rap1 in integrin-mediated cell adhesion. Biochem Soc Trans 31: 83-86, 2003.
18. Wang C, Wu C, Yang Q, Ding M, Zhong J, Zhang CY, Ge J, Wang J and Zhang C: miR-28-5p acts as a tumor suppressor in renal cell carcinoma for multiple antitumor effects by targeting RAP1B. Oncotarget 7: 73888-73902, 2016.
19. Peng H, Luo J, Hao H, Hu J, Xie S, Ren D, Song C and Peng X: MicroRNA-100 regulates SW620 colorectal cancer cell proliferation and invasion by targeting RAP1B. Oncol Rep 31: 2055-2062, 2014.
20. Yang Y, Li M, Yan Y, Zhang J, Sun K, Qu J and Xu Y: Expression of RAP1B is associated with poor prognosis and promotes an aggressive phenotype in gastric cancer. Oncol Rep 34: 2385-2394, 2015.
21. Livak KJ and Schmittgen TD: Analysis of relative gene expression data using real-time quantitative PCR and the 2(-Delta Delta C(T)) method. Methods 25: 402-408, 2001.
22. Kondo R, Ishino K, Wada R, Takata H, Peng WX, Kudo M, Naito Z and Wada S: Downregulation of protein disulfide isomerase A3 expression inhibits cell proliferation and induces apoptosis through STAT3 signaling in hepatocellular carcinoma. Int J Oncol 54: 1409-1421, 2019.
23. Ishino K, Kudo M, Peng WX, Kure S, Kawahara K, Teduka K, Kawamoto Y, Fujii T and Naito Z: 2-Deoxy-d-glucose increases GFAT1 phosphorylation resulting in endoplasmic reticulum-related apoptosis via disruption of protein N-glycosylation in pancreatic cancer cells. Biochem Biophys Res Commun 501: 668-673, 2018.
24. Old WM, Meyer-Arendt K, Aveline-Wolf L, Pierce KG, Mendoza A, Sevinsky JR, Resing KA and Ahn NG: Comparison of label-free methods for quantifying human proteins by shotgun proteomics. Mol Cell Proteomics 4: 1487-1502, 2005.
25. Otake H, Yamamoto T, Deguchi S, Taga A and Nagai N: Retinal proteomic evaluation of rats following streptozotocin-injection using shotgun proteomics. Mol Med Rep 21: 379-386, 2020.
26. Kanehisa M and Goto S: KEGG: Kyoto encyclopedia of genes and genomes. Nucleic Acids Res 28: 27-30, 2000.
27. Stringer C, Wang T, Michaelos M and Pachitariu M: Cellpose: A generalist algorithm for cellular segmentation. Nat Methods 18: 100-106, 2021.
28. Han Q, Li J, Xiong J and Song Z: Long noncoding RNA LINC00514 accelerates pancreatic cancer progression by acting as a ceRNA of miR-28-5p to upregulate Rap1b expression. J Exp Clin Cancer Res 39: 151, 2020.
29. Wang A, Dai H, Gong Y, Zhang C, Shu J, Luo Y, Luo H, Liu Z and Liu L: ANLN-induced EZH2 upregulation promotes pancreatic cancer progression by mediating miR-218-5p/LASP1 signaling axis. J Exp Clin Cancer Res 38: 347, 2019.
30. Öhlund D, Handly-Santana A, Biffi G, Elyada E, Almeida AS, Ponz-Sarvise M, Corbo V, Oni TE, Hearn SA, Lee EJ, *et al*: Distinct populations of inflammatory fibroblasts and myofibroblasts in pancreatic cancer. J Exp Med 214: 579-596, 2017.
31. Mizutani Y, Kobayashi H, Iida T, Asai N, Masamune A, Hara A, Esaki N, Ushida K, Mii S, Shiraki Y, *et al*: Meflin-positive cancer-associated fibroblasts inhibit pancreatic carcinogenesis. Cancer Res 79: 5367-5381, 2019.
32. Miyai Y, Sugiyama D, Hase T, Asai N, Taki T, Nishida K, Enomoto A, Yokoi K and Nagino M: Meflin-positive cancer-associated fibroblasts enhance tumor response to immune checkpoint blockade. Life Sci Alliance 5: e202101230, 2022.
33. Ishii N, Araki K, Yokobori T, Hagiwara K, Gantumur D, Yamanaka T, Tsukagoshi M, Igarashi T, Watanabe A, Kubo N, *et al*: Conophylline suppresses pancreatic cancer desmoplasia and cancer-promoting cytokines produced by cancer-associated fibroblasts. Cancer Sci 110: 334-344, 2019.
34. Yonemura H, Kuwatani M, Nakajima K, Masamune A, Ogawa M and Sakamoto N: Treatment of pancreatic cancer using near-infrared photoimmunotherapy targeting cancer-associated fibroblasts in combination with anticancer chemotherapeutic drug. Cancers (Basel) 17: 1584, 2025.
35. Tsunetoshi Y, Sanada F, Kanemoto Y, Shibata K, Masamune A, Taniyama Y, Rakugi H and Morishita R: A role for periostin pathological variants and their interaction with HSP70-1a in promoting pancreatic cancer progression and chemoresistance. Int J Mol Sci 25: 13205, 2024.
36. Leca J, Martinez S, Lac S, Nigri J, Secq V, Rubis M, Bressy C, Sergé A, Lavaut MN, Dusetti N, *et al*: Cancer-associated fibroblast-derived annexin A6+ extracellular vesicles support pancreatic cancer aggressiveness. J Clin Invest 126: 4140-4156, 2016.

37. Cao W, Zeng Z, He Z and Lei S: Hypoxic pancreatic stellate cell-derived exosomal miRNAs promote proliferation and invasion of pancreatic cancer through the PTEN/AKT pathway. Aging (Albany NY) 13: 7120-7132, 2021.
38. Richards KE, Xiao W, Hill R, Herring BP, Li H, Gunawardena HP, Bhaskara S, Bhatt DL and O'Brien P: Cancer-associated fibroblasts confer gemcitabine resistance to pancreatic cancer cells through PTEN-targeting miRNAs in exosomes. Cancers (Basel) 14: 2812, 2022.
39. KEGG PATHWAY: Focal adhesion (hsa04510). https://www.kegg.jp/pathway/hsa04510 (Accessed July 12, 2025).
40. KEGG PATHWAY: Renal cell carcinoma (hsa05211). https://www.kegg.jp/pathway/hsa05211 (Accessed July 12, 2025).
41. Katagiri K and Kinashi T: Rap1 and integrin inside-out signaling. Methods Mol Biol 757: 279-296, 2012.
42. Huang M, Anand S, Murphy EA, Desgrosellier JS, Stupack DG, Shattil SJ and Bhatt DL: EGFR-dependent pancreatic carcinoma cell metastasis through Rap1 activation. Oncogene 31: 2783-2793, 2012.
43. Tang Z, Peng H, Chen J, Zheng X and Zhang X: Rap1b enhances the invasion and migration of hepatocellular carcinoma cells by up-regulating Twist1. Exp Cell Res 367: 56-64, 2018.
44. Jia Z, Yang Y, Zhang D, Guo M, Zhao Y, Yu J, Zeng Y and Xue Y: RAP1B, a DVL2-binding protein, activates Wnt/β-catenin signaling in esophageal squamous cell carcinoma. Gene 611: 15-20, 2017.
45. D'Avino PP: How to scaffold the contractile ring for a safe cytokinesis-lessons from Anillin-related proteins. J Cell Sci 122: 1071-1079, 2009.
46. Naydenov NG, Koblinski JF and Ivanov AI: Anillin is an emerging regulator of tumorigenesis, acting as a cortical cytoskeletal scaffold and a nuclear modulator of cancer cell differentiation. Cell Mol Life Sci 78: 621-633, 2021.
47. Idichi T, Seki N, Kurahara H, Yonemori K, Osako Y, Arai T, Kita Y, Yoshiura T, Mataki Y, Maemura K, *et al*: Regulation of actin-binding protein ANLN by antitumor miR-217 inhibits cancer cell aggressiveness in pancreatic ductal adenocarcinoma. Oncotarget 8: 53180-53193, 2017.
48. Sugiura R, Satoh R and Takasaki T: ERK: A double-edged sword in cancer. ERK-dependent apoptosis as a potential therapeutic strategy for cancer. Cells 10: 2509, 2021.
49. Burge RA, Bialousow L, McFall T, Bamonte L, Johnson G, Smith M, Vaena SG, Comte-Walters S, Ball LE, Berto S, *et al*: Pancreatic cells are resistant to KRAS Q61L expression due to hyperactive ERK/MAPK signaling and apoptosis induction. Cancer Res Commun 5: 1865-1879, 2025.
50. Rowell MC, Deschênes-Simard X, Lopes-Paciencia S, Le Calvé B, Kalegari P, Mignacca L, Fernandez-Ruiz A, Guillon J, Lessard F, Bourdeau V, *et al*: Targeting ribosome biogenesis reinforces ERK-dependent senescence in pancreatic cancer. Cell Cycle 22: 2172-2193, 2023.
51. Nussinov R, Jang H, Zhang M, Tsai CJ and Sablina AA: The mystery of Rap1 suppression of oncogenic Ras. Trends Cancer 6: 369-379, 2020.
52. Wang L, Wang J, Wang N, Wang X, Song M, Zhou Y, Wang Z, Meng H, Guo E and Miao S: ANLN promotes head and neck squamous cell carcinoma progression by upregulating PD-L1 via the ERK-MAPK pathway. iScience 28: 111633, 2024.
53. Liu Y, Cao P, Cao F, Wang S, He Y, Xu Y and Wang Y: ANLN, regulated by SP2, promotes colorectal carcinoma cell proliferation via PI3K/AKT and MAPK signaling pathway. J Invest Surg 35: 268-277, 2021.
54. Ewald B, Sampath D and Plunkett W: H2AX phosphorylation marks gemcitabine-induced stalled replication forks and S-phase checkpoint activation. Mol Cancer Ther 6: 1239-1248, 2007.

Copyright © 2026 Yoshimori et al. This work is licensed under a Creative Commons Attribution-NonCommercial-NoDerivatives 4.0 International (CC BY-NC-ND 4.0) License.